

## Article

# Approximating Dynamic Elastic Modulus of Concrete for an Old Aqueduct Using Dynamic Tests and BP Neural Network

Xiaobin Lu <sup>1,2,3</sup>, Xiulin Li <sup>1,2,3,\*</sup> , Jun Xiao <sup>1,2,3</sup> and Meng Li <sup>1,2,3</sup><sup>1</sup> State Key Laboratory of Simulation and Regulation of Water Cycle in River Basin, Beijing 100038, China; xluttnj@yahoo.com (X.L.); xiaoj@iwhr.com (J.X.); limeng@iwhr.com (M.L.)<sup>2</sup> Division of Materials, China Institute of Water Resources and Hydropower Research, Beijing 100038, China<sup>3</sup> Key Laboratory of Engineering Materials of Ministry of Water Resources, Beijing 100038, China

\* Correspondence: lixl@iwhr.com; Tel.: +86-13552059878

**Abstract:** Monitoring the degradation of the dynamic elastic modulus ( $E_d$ ) of concrete is of great importance to track the durability deterioration for hydraulic concrete structures. For the aqueduct under investigation in this study, the dynamic elastic modulus of bent frames and moment frame supports ( $E_{d-frame}$ ), the dynamic elastic modulus of arch trusses ( $E_{d-arch}$ ) and the shear stiffnesses of the asphaltic bearings of U-shaped flumes ( $K_{flume}$ ) are the main parameters to define the dynamic behavior of the structure, which have direct correlation with its vibrational characteristics and thus practicably can be estimated by a BP (back-propagation) neural network using modal frequencies as inputs. Since it is impossible to obtain sufficient experimental field data to train the network, a full-scale 3D FE model of the entire aqueduct is created, and modal analyses under different combinations of  $K_{flume}$ ,  $E_{d-arch}$  and  $E_{d-frame}$  are conducted to generate the analytical dataset for the network. After the network's architecture is refined by the cross-validation process and its modeling accuracy verified by the test procedure, the primary modal frequencies of the aqueduct obtained from in situ dynamic tests are put into the network to obtain the final approximations for  $K_{flume}$ ,  $E_{d-arch}$  and  $E_{d-frame}$ , which sets an evaluation baseline of the general concrete  $E_d$  status for the aqueduct and indicates that the makeshift asphaltic bearings of U-shaped flumes basically can be treated as a three-directional hinge in the FE model. It is also found that more inputs of modal frequencies can improve the prediction accuracy of the BP neural network.



**Citation:** Lu, X.; Li, X.; Xiao, J.; Li, M. Approximating Dynamic Elastic Modulus of Concrete for an Old Aqueduct Using Dynamic Tests and BP Neural Network. *Appl. Sci.* **2023**, *13*, 8367. <https://doi.org/10.3390/app13148367>

Academic Editor: Andrea Prati

Received: 19 June 2023

Revised: 14 July 2023

Accepted: 17 July 2023

Published: 19 July 2023



**Copyright:** © 2023 by the authors. Licensee MDPI, Basel, Switzerland. This article is an open access article distributed under the terms and conditions of the Creative Commons Attribution (CC BY) license (<https://creativecommons.org/licenses/by/4.0/>).

## 1. Research Background

A large concrete aqueduct with a total length of 1083.6 m is a key structure of a water supply project in eastern China. It has 21 spans with a 51.6 m equal span length. The structural feature of the aqueduct is shown in Figure 1, and its main load-bearing components are comprised of arch trusses (concrete design strength C50), bent frames (C40) and moment frame supports (C40). The aqueduct was built in 2006, and after 17 years of operation without any safety monitoring measures, the management now plans to install an SHM on it.

The dynamic elastic modulus ( $E_d$ ) of concrete is of great interest in hydraulic structures. In the Chinese hydraulic concrete design code, the durability of concrete is evaluated by the reduction of  $E_d$ , which can also provide appropriate dynamic parameters for the seismic analysis [1,2]. For high-, normal- and low-strength concrete, the ratios of the dynamic-to-static elastic modulus ( $E_d/E_c$ ) are around 1.2, 1.3 and 1.4, respectively [1]. According to the dynamic equilibrium equation, the natural vibration frequencies of a concrete structure are directly related to its concrete  $E_d$ , which can be obtained from examining the dynamic responses of the structure on site.



**Figure 1.** Main structural feature of the arch-truss aqueduct.

Aqueducts are structurally similar, with bridges. Vibration-based (dynamic) tests have been considered as an effective approach to evaluate the structural health of bridges [3]. Many previous studies focused on analyzing modal parameters (frequencies and shapes) through numerical models combined with field test results to identify and locate structural damages in bridges [4–8]. Analyses of modal parameters were performed to assess significant negative effects on bridges due to structural rehabilitation [9,10], and some researchers conducted ambient and vehicle-induced vibration tests for a real bridge subject to various deliberately designed damage conditions [11]. Besides full-scale applications, vibration tests were also used to evaluate local damages in decks and slab–girder connectors of bridges [12–14] and assist in optimizing the boundary constraints of the structural FE models [15]. In recent years, more researchers have employed machine learning, especially artificial neural networks, in the damage detection of bridges by exploiting in situ experimental and numerical analytical data [16–19], and particularly due to its maturity in both theory and performance as well as flexibility in network architecture, BP (back-propagation) neural network has been widely used [20–23]. Efforts have also been made in applying convolutional neural networks (CNNs) to visually reveal structural defects in bridge girders [24,25].

The purpose of this study was to determine the general concrete  $E_d$  status for the main load-bearing components (arch trusses, bent frames and moment frame supports) of the aqueduct, thus to set an evaluation baseline before the SHM implementation. So with the long-term concrete  $E_d$  data accumulated from the subsequent monitoring, it is possible to track the development of the health status of this old aqueduct. This task is completed by the application of in situ dynamic tests and the BP neural network trained with analytical data from a full-scale numerical model (see Figure 2), as discussed below.

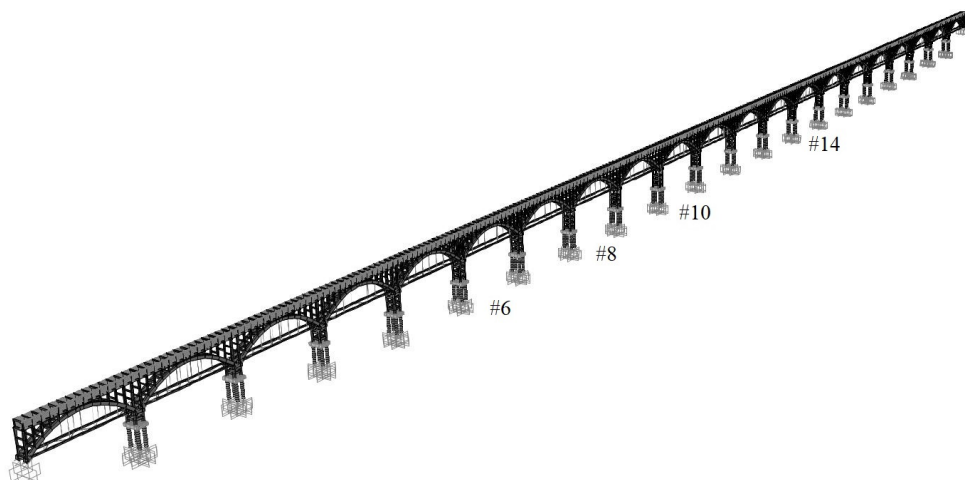


**Figure 2.** Full-scale 3D FE model of the aqueduct.

## 2. Dynamic Tests of the Real Structure

In situ dynamic tests were performed to investigate the structural vibration characteristics of the aqueduct under the natural wind excitation. Velocity transducers were installed on the top surface of the bottom slabs of the U-shaped flumes at locations of 1/4, 1/2 and 3/4 spans for span 6, 8, 10 and 14 (see Figure 2). A three-directional transducer layout, as shown in Figure 3, was adopted at the 1/2 span along the lateral, longitudinal and vertical directions, whereas only lateral and longitudinal transducers were placed at 1/4 and 3/4 spans. The 4 spans were tested individually. A sampling frequency of 20 Hz, which corresponds to a sampling interval of 50 ms, was set, and the total sampling time was fixed as 10 min. In the final data processing, an FFT point of 4096, Hanning window and 1/2 data-segment overlap were chosen, which gave rise to a 0.005 Hz resolution in the frequency domain spectra. Under the aforementioned testing setups and analysis parameters, the velocity spectra in the frequency domain for all transducers in three directions of the 4 spans are shown in Figures 4–7. To better show the consistency of test results, two typical spectra obtained from 3 lateral sensors (@ 1/4, 1/2 and 3/4 span) on span #8 and #10 are also provided (see Figures 8 and 9). On the velocity spectrum of each span, the peak amplitude frequencies obtained from the data collected by more than 2 transducers in the same direction (lateral or longitudinal) but at different locations well coincide with one another.



**Figure 3.** Transducer layout inside U-shaped flumes.

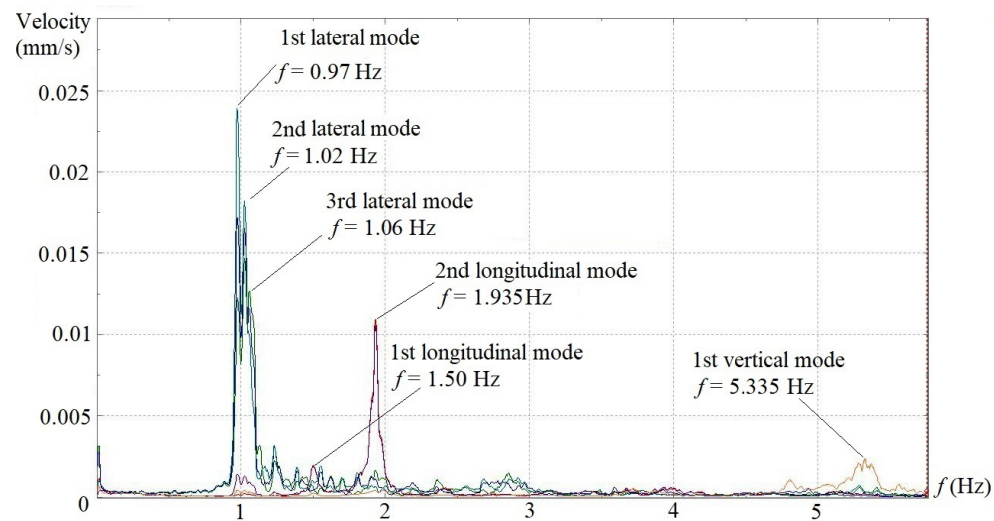


**Figure 4.** Velocity spectrum in frequency domain of span #6.

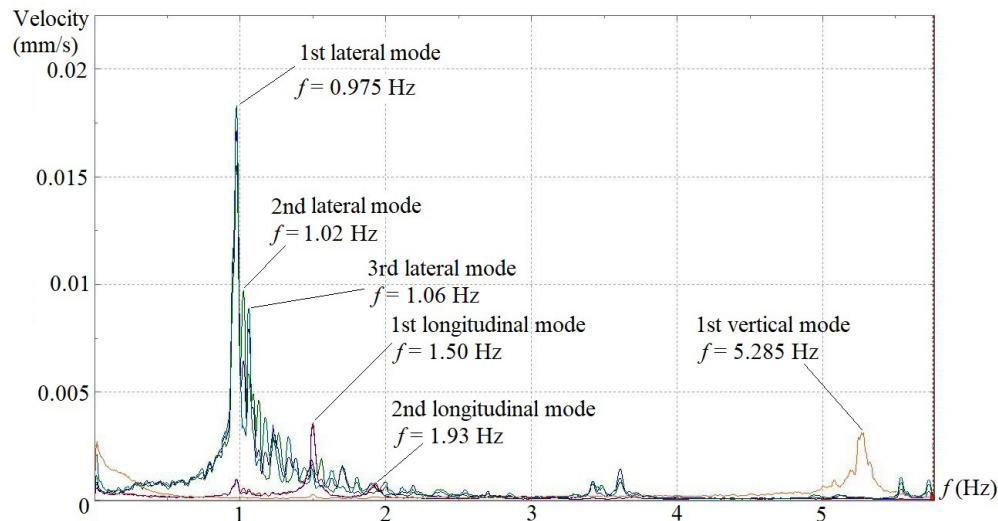


**Figure 5.** Velocity spectrum in frequency domain of span #8.

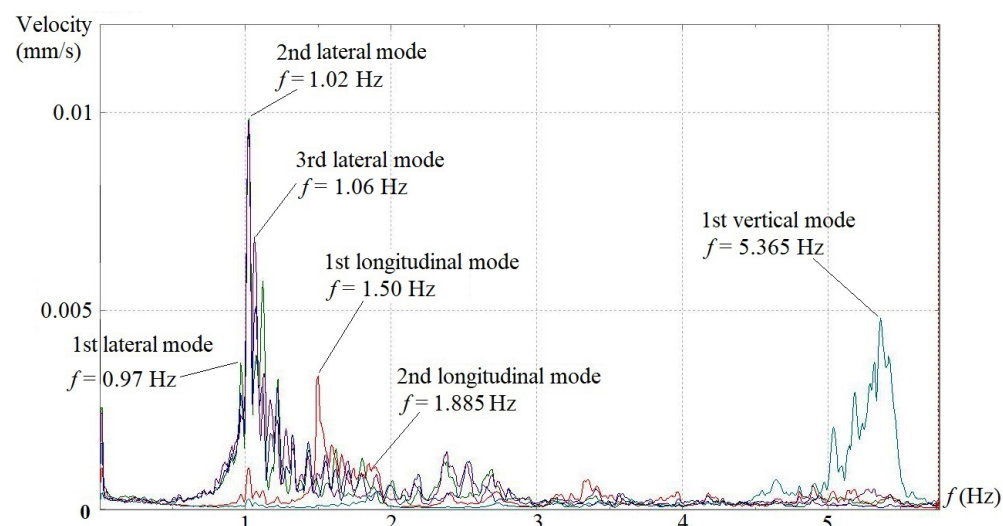


**Figure 6.** Velocity spectrum in frequency domain of span #10.

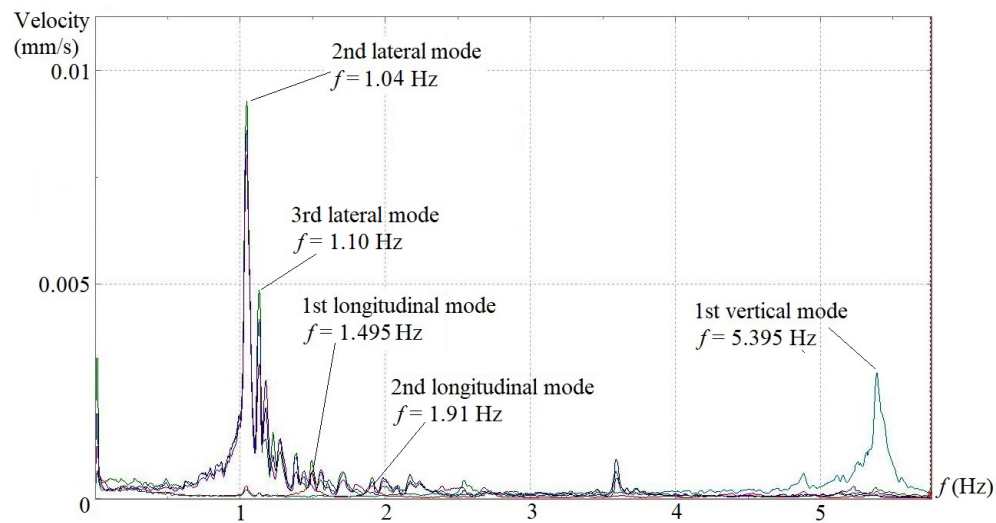


**Figure 7.** Velocity spectrum in frequency domain of span #14.

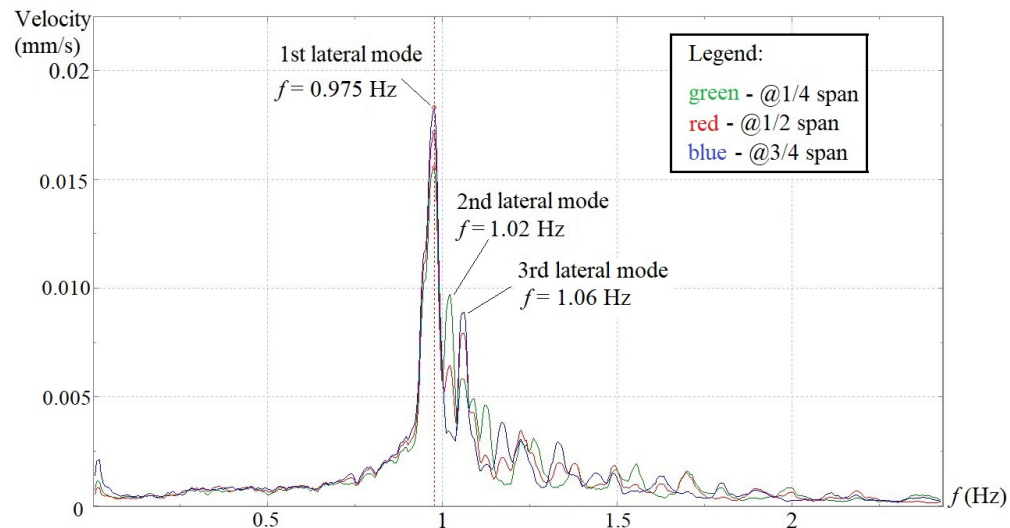


**Figure 8.** Velocity spectrum of 3 lateral transducers for span #8.

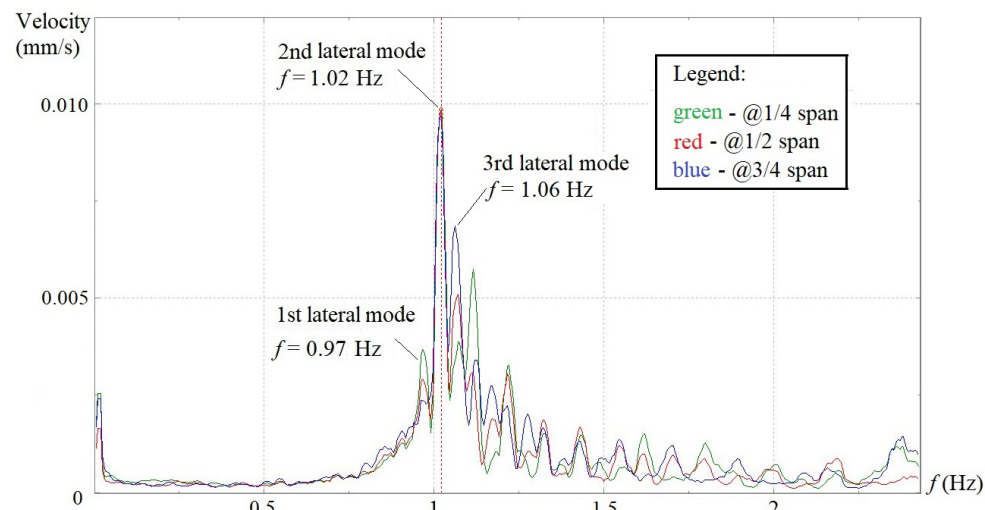


**Figure 9.** Velocity spectrum of 3 lateral transducers for span #10.

It is obvious that the lateral vibration of the aqueduct is dominant among three directions, with its velocity amplitudes being higher than those along the longitudinal and vertical directions. Span 6 and span 8 essentially demonstrate the same lateral vibration feature in which the frequencies of the first, second and third lateral modes stand at 0.97~0.975 Hz, 1.02 Hz and 1.06 Hz, respectively, and the first mode has much higher velocity amplitude than the other two. Span 10 has the same lateral mode frequencies with span 6 and span 8, but contrary to the two former spans, the velocity amplitude of the first mode is lower than those of the second and third modes. Span 14 does not show the first lateral mode at 0.97 Hz on the velocity spectrum, but two other peak amplitudes appear at 1.04 Hz and 1.10 Hz, which are quite close to the second and third lateral modes of the other three spans. Although the four sets of results cannot be compared with one another directly since dynamic tests were conducted individually for each span, a general trend can still be observed that the lateral velocity amplitudes of span 6 and span 8 are much higher than those corresponding values of span 10 and span 14.

The longitudinal vibration of the aqueduct basically exhibits two main modes on the four velocity spectra. The frequencies of the first longitudinal modes locate consistently at 1.495~1.50 Hz, while the second longitudinal modes fluctuate within a very small range of 1.885~1.935 Hz. Unlike the lateral and longitudinal vibrations, the vertical vibration of the aqueduct only manifests a single peak frequency around 5.285~5.395 Hz on the velocity spectra of all four spans, with the velocity amplitudes maintaining at almost the same magnitude.

From those field test findings, the dynamic characteristics of the whole aqueduct can be summarized in Table 1.

**Table 1.** Dynamic characteristics of the aqueduct from field tests.

| Modes              | Times  | Frequency (Hz) |
|--------------------|--------|----------------|
| Lateral modes      | first  | 0.97           |
|                    | second | 1.02           |
|                    | third  | 1.06           |
| Longitudinal modes | first  | 1.50           |
|                    | second | 1.915 *        |
| Vertical mode      | first  | 5.328 *        |

\* average of span 6, 8 and 10.

### 3. Modal Analysis of the 3D Aqueduct Model

A 3D FE model is established using SAP2000 for the entire aqueduct, as shown in Figure 2. The arch trusses, transverse bent frames above those trusses, moment frame supports and foundation piles are generated by frame elements, and the water-transferring U-shaped flumes and pile foundation caps are created using shell elements. A 3 cm-wide contraction joint is set between two adjacent U-shaped flume segments. The pot-type fixed rubber bearing of the arch trusses at the upstream end of each span is simulated as a rubber isolator restrained in all translational and rotational DOFs, while the pot-type sliding counterpart at the downstream end of each span is modeled with the same DOF restraints except that the shear stiffness in the longitudinal translation is set to be zero.

The interaction between foundation piles and surrounding soil is simulated with node springs using “m” method. According to the current Chinese code “Technical Code for Building Pile Foundations (JGJ 94-2008) [26]”, the lateral stiffness of the node spring of a pile can be calculated as follows:

$$K = ab_0mZ \quad (1)$$

where  $K$  is the lateral stiffness of the node spring ( $\text{kN}/\text{m}$ );  $a$  is the thickness of the foundation soil layer, normally taken as 1~2 m;  $b_0$  is the effective width of the pile (m), and when the pile diameter  $d$  is larger than 1 m,  $b_0 = 0.9 \times (d + 1)$ ;  $Z$  is the depth of the foundation

soil layer (m); and  $m$  represents the proportional coefficient of horizontal resistance of foundation soil ( $\text{kN}/\text{m}^4$ ), and for cast-in-place concrete piles can be taken as shown in Table 2 for different foundation soils (in this case, it can be taken as  $100\sim300 \text{ MN}/\text{m}^4$ ).

**Table 2.** “ $m$ ” value for different nonrock foundation soils.

| Foundation Soils                      | “ $m$ ” Value/ $\text{kN}/\text{m}^4$ |
|---------------------------------------|---------------------------------------|
| Silt and silty clay                   | $2.5 \times 10^3\sim6 \times 10^3$    |
| Loose sand and earth fill             | $6 \times 10^3\sim14 \times 10^3$     |
| Medium-dense earth fill and fine sand | $14 \times 10^3\sim35 \times 10^3$    |
| Medium-dense medium-coarse sand       | $35 \times 10^3\sim100 \times 10^3$   |
| Dense coarse sand and gravels         | $100 \times 10^3\sim300 \times 10^3$  |

In the real structure, the prefabricated U-shaped concrete flume segments are laid directly on the top beams of transverse bent frames erected on the arch trusses, but the bearings only adopt two layers of thin (about 1 mm thickness) asphaltic felts instead of commonly used plate rubber supports. In the 3D model, this makeshift asphaltic bearing is simulated by an elastic link element restrained in vertical translation and rotation about the vertical axis while free in the other two rotational DOFs, but the shear stiffnesses in the transverse and longitudinal directions need to be defined, which can be assumed to be equal based on the empirical equation:

$$K = GA/t \quad (2)$$

where  $K$  is the bearing shear stiffness,  $G$  is the shear modulus of the bearing material,  $A$  is the plane area of the bearing, and  $t$  is the bearing thickness.

The influence of the “ $m$ ” value variation of foundation soil on the dynamic characteristics of the aqueduct was investigated. In this case, certain dynamic elastic moduli are assumed for arch trusses (40 GPa), bent frames (37.5 GPa), moment frame supports (37.5 GPa), pile caps and piles (32.5 GPa) in the 3D model based on their respective design strengths, and the shear stiffnesses of asphaltic bearings of U-shaped flumes in both transverse and longitudinal directions are set to be  $1.536 \times 10^7 \text{ kN}/\text{m}$ . The modal analysis results are listed in Table 3. It can be seen that the change of the “ $m$ ” value in a code-specified range has an insignificant impact on the dynamic characteristics of the aqueduct.

**Table 3.** Primary modal frequencies (Hz) of the aqueduct under different “ $m$ ”.

| $m$ ( $\text{MN}/\text{m}^4$ ) | Lateral Modes |        |       | Longitudinal Modes |        | Vertical Mode |
|--------------------------------|---------------|--------|-------|--------------------|--------|---------------|
|                                | First         | Second | Third | First              | Second | First         |
| 300                            | 0.884         | 0.934  | 0.944 | 1.297              | 1.576  | 4.942         |
| 100                            | 0.880         | 0.929  | 0.939 | 1.282              | 1.554  | 4.940         |

By altering one of those parameters while keeping others unchanged, the sensitivity analyses of dynamic elastic moduli of arch trusses ( $E_{d\text{-arch}}$ ), bent frames, moment frame supports ( $E_{d\text{-frame}}$ ), pile caps and piles ( $E_{d\text{-pile}}$ ) on the dynamic characteristics of the aqueduct are conducted, and the results are shown in Tables 4–6. It can be seen that under almost the same variation,  $E_{d\text{-pile}}$  has much less influence compared with  $E_{d\text{-arch}}$  and  $E_{d\text{-frame}}$ , which may be attributed to the large rigidity of the foundation (i.e., pile cap thickness 1.5 m and pile diameter 1.5 m). It is also found that the vertical frequency is sensitive to  $E_{d\text{-arch}}$ , while the lateral and longitudinal frequencies are sensitive to  $E_{d\text{-frame}}$ .

**Table 4.** Dynamic characteristics of the aqueduct under different  $E_{d\text{-pile}}$ .

| $E_{d\text{-arch}}$<br>/GPa | $E_{d\text{-frame}}$<br>/GPa | $E_{d\text{-pile}}$<br>/GPa | Primary Modal Frequencies/Hz |       |       |              |       |          |
|-----------------------------|------------------------------|-----------------------------|------------------------------|-------|-------|--------------|-------|----------|
|                             |                              |                             | Lateral                      |       |       | Longitudinal |       | Vertical |
|                             |                              |                             | 1st                          | 2nd   | 3rd   | 1st          | 2nd   | 1st      |
| 40                          | 37.5                         | 32.5                        | 0.884                        | 0.934 | 0.944 | 1.297        | 1.576 | 4.942    |
| 40                          | 37.5                         | 40                          | 0.896                        | 0.947 | 0.957 | 1.318        | 1.596 | 4.962    |
| +0%                         | +0%                          | +23.1%                      | +1.4%                        | +1.4% | +1.4% | +1.6%        | +1.3% | +0.4%    |

**Table 5.** Dynamic characteristics of the aqueduct under different  $E_{d\text{-arch}}$ .

| $E_{d\text{-arch}}$<br>/GPa | $E_{d\text{-frame}}$<br>/GPa | $E_{d\text{-pile}}$<br>/GPa | Primary Modal Frequencies/Hz |       |       |              |       |          |
|-----------------------------|------------------------------|-----------------------------|------------------------------|-------|-------|--------------|-------|----------|
|                             |                              |                             | Lateral                      |       |       | Longitudinal |       | Vertical |
|                             |                              |                             | 1st                          | 2nd   | 3rd   | 1st          | 2nd   | 1st      |
| 40                          | 37.5                         | 32.5                        | 0.884                        | 0.934 | 0.944 | 1.297        | 1.576 | 4.942    |
| 50                          | 37.5                         | 32.5                        | 0.899                        | 0.952 | 0.963 | 1.308        | 1.593 | 5.363    |
| +25.0%                      | +0%                          | +0%                         | +1.7%                        | +1.9% | +2.0% | +0.8%        | +1.1% | +8.5%    |

**Table 6.** Dynamic characteristics of the aqueduct under different  $E_{d\text{-frame}}$ .

| $E_{d\text{-arch}}$<br>/GPa | $E_{d\text{-frame}}$<br>/GPa | $E_{d\text{-pile}}$<br>/GPa | Primary Modal Frequencies/Hz |       |       |              |       |          |
|-----------------------------|------------------------------|-----------------------------|------------------------------|-------|-------|--------------|-------|----------|
|                             |                              |                             | Lateral                      |       |       | Longitudinal |       | Vertical |
|                             |                              |                             | 1st                          | 2nd   | 3rd   | 1st          | 2nd   | 1st      |
| 40                          | 37.5                         | 32.5                        | 0.884                        | 0.934 | 0.944 | 1.297        | 1.576 | 4.942    |
| 40                          | 46.5                         | 32.5                        | 0.950                        | 1.001 | 1.012 | 1.398        | 1.698 | 5.029    |
| +0%                         | +24.0%                       | +0%                         | +7.5%                        | +7.2% | +7.2% | +7.8%        | +7.7% | +1.8%    |

The flumes have the same design strength (C40) with bent frames and moment frame supports, so in the modal analysis, the dynamic elastic modulus  $E_{d\text{-flume}}$  is assigned to be the same with  $E_{d\text{-frame}}$ . Following the same procedure, the impact of  $E_{d\text{-flume}}$  variation on the dynamic characteristics of the aqueduct was also investigated and found to be minor, as shown in Table 7.

**Table 7.** Dynamic characteristics of the aqueduct under different  $E_{d\text{-flume}}$ .

| $E_{d\text{-arch}}$<br>/GPa | $E_{d\text{-frame}}^*$<br>/GPa | $E_{d\text{-pile}}$<br>/GPa | Primary Modal Frequencies/Hz |       |       |              |       |          |
|-----------------------------|--------------------------------|-----------------------------|------------------------------|-------|-------|--------------|-------|----------|
|                             |                                |                             | Lateral                      |       |       | Longitudinal |       | Vertical |
|                             |                                |                             | 1st                          | 2nd   | 3rd   | 1st          | 2nd   | 1st      |
| 40                          | 37.5                           | 32.5                        | 0.884                        | 0.934 | 0.944 | 1.297        | 1.576 | 4.942    |
| 40                          | 46.5 *                         | 32.5                        | 0.885                        | 0.936 | 0.946 | 1.313        | 1.615 | 4.948    |
| +0%                         | +24.0%                         | +0%                         | +0.1%                        | +0.2% | +0.2% | +1.2%        | +2.5% | +0.1%    |

\*  $E_{d\text{-frame}}$  is kept as 37.5 GPa.

Therefore, after neglecting those two parameters, the main parameters left that may affect the dynamic characteristics of the 3D aqueduct model are the shear stiffnesses of the asphaltic bearings of U-shaped flumes, the dynamic elastic modulus of arch trusses (concrete design strength C50), and the dynamic elastic modulus of bent frames and moment frame supports (C40). By arranging those 3 parameters into various combinations, a series of modal analyses of the aqueduct are performed, and the typical primary mode shapes are shown in Figures 10–15.

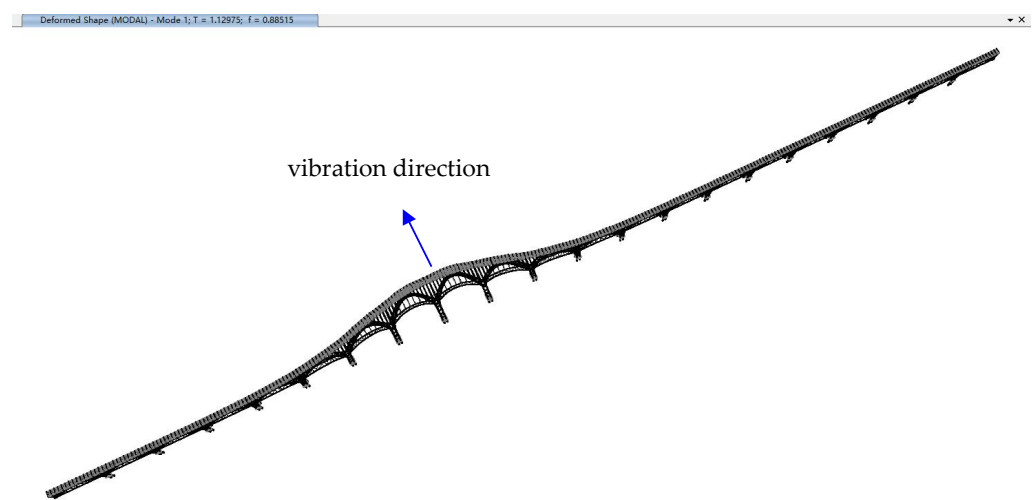


**Figure 10.** Typical first lateral vibration mode of the aqueduct.

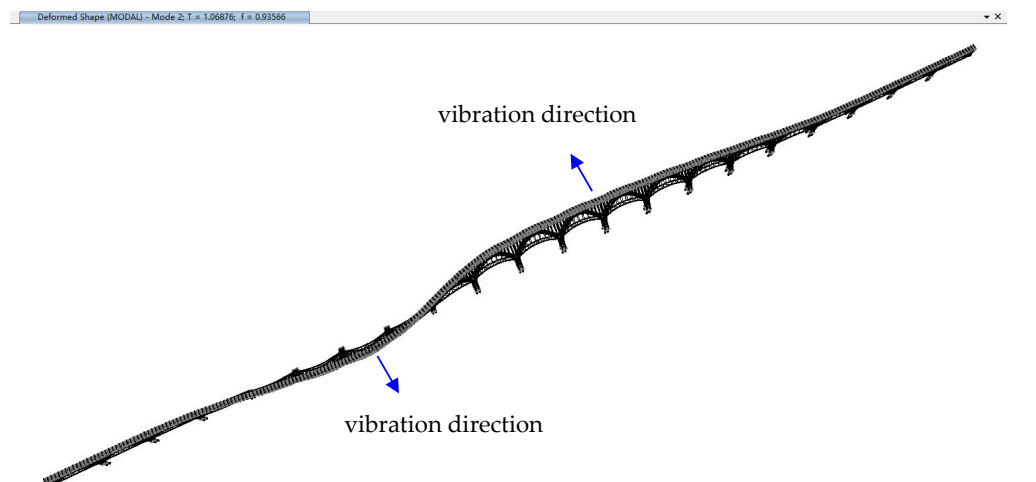


**Figure 11.** Typical second lateral vibration mode of the aqueduct.

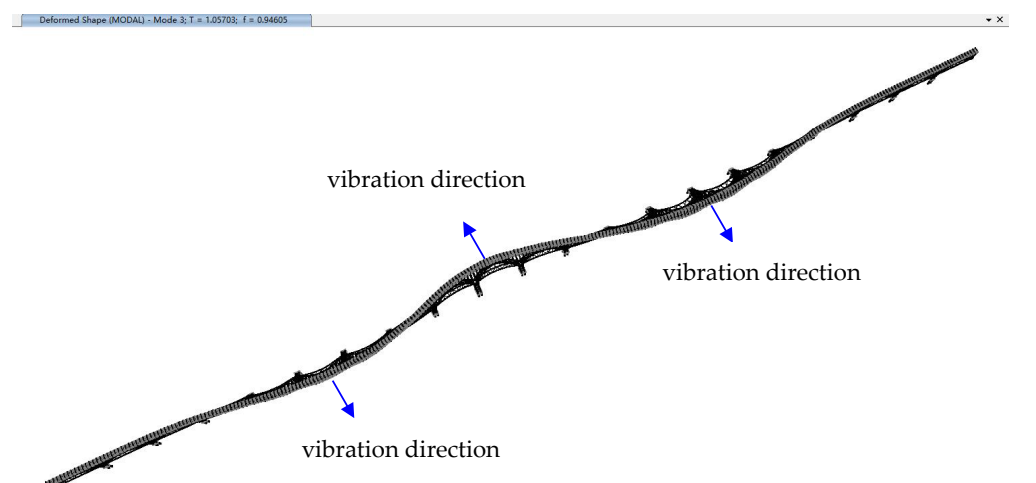


**Figure 12.** Typical third lateral vibration mode of the aqueduct.

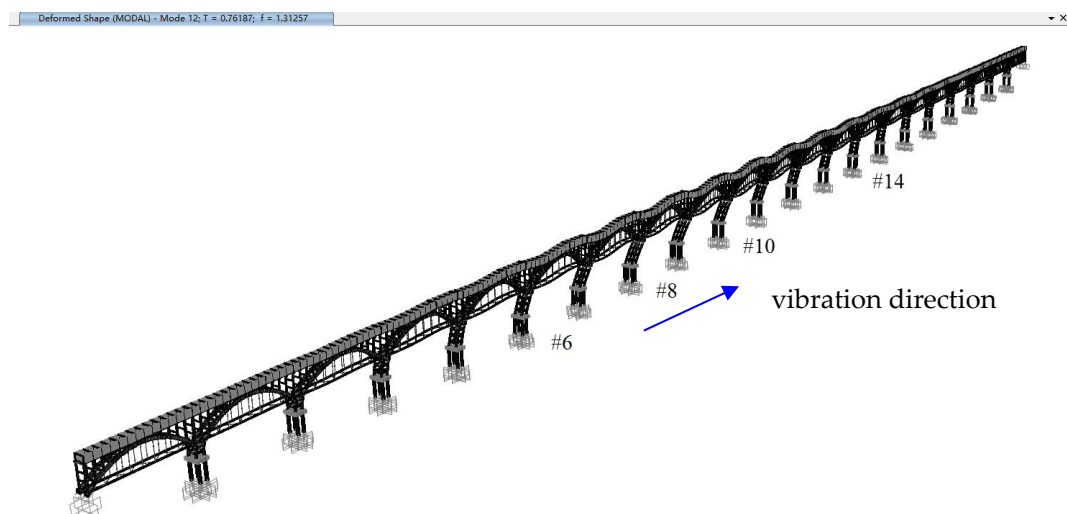


**Figure 13.** Typical first longitudinal vibration mode of the aqueduct.

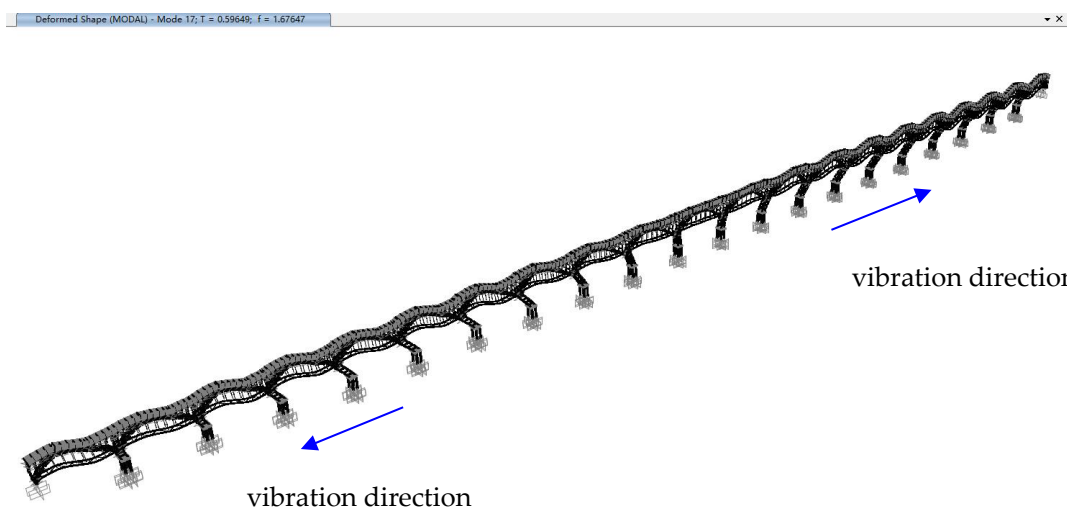


**Figure 14.** Typical second longitudinal vibration mode of the aqueduct.

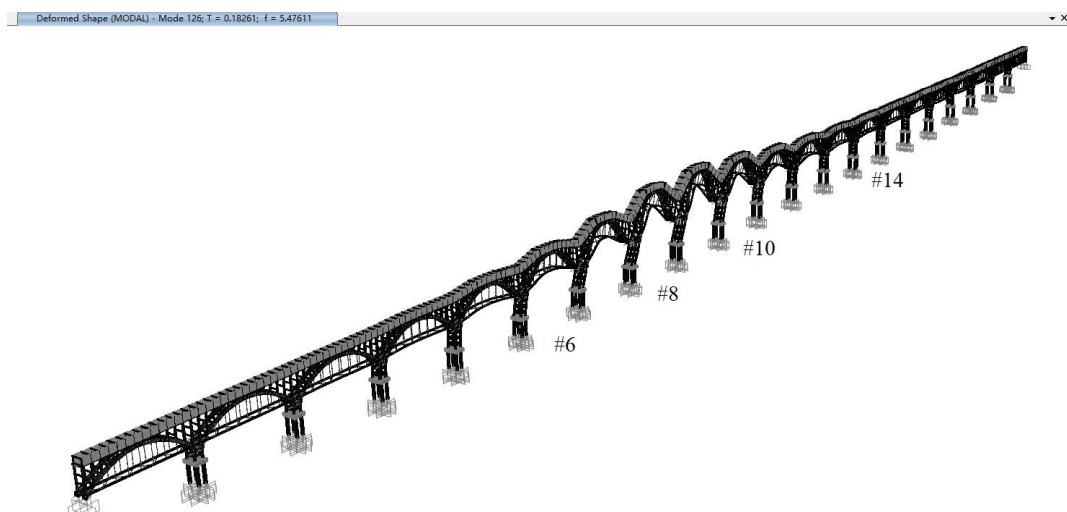


**Figure 15.** Typical first (primary) vertical vibration mode of the aqueduct.

The first lateral modes of the aqueduct for all analysis scenarios have modal participating mass ratios nearing 20%, which are higher than those of other lateral modes. As shown in Figure 10, the first lateral mode typically manifests itself as a lateral vibration of some interior spans (i.e., span 6 to span 11) in the same direction, whereas the motions of exterior spans including span 14 are not activated, which may justify the missing of the first lateral mode on the velocity spectrum of span 14 (see Figure 7). It can be seen from Figures 11 and 12 that the second and third lateral modes involve transverse vibration of more spans including span 6, 8, 10 and 14, which conforms to the appearances of these two modes on all velocity spectra obtained from field dynamic tests (see Figures 4–7).

As shown in Figures 13 and 14, the first (normally with a modal participating mass ratio around 20~50%) and second longitudinal modes of the aqueduct for all analysis scenarios both show longitudinal vibration of most spans concurrently, which also accords with the presence of two longitudinal peak frequencies in Figures 4–7.

The first vertical modes of the aqueduct for all analysis scenarios have modal participating mass ratios around 20%, typically displaying a simultaneous vertical vibration shape of arch trusses in most interior spans, as shown in Figure 15. In fact, there still exist one or two similar vertical modes which have slightly lower or higher frequencies but much less modal participation mass ratios than that primary mode, and this may explain the small differences of the first vertical mode frequencies obtained from the field dynamic tests of the four spans, as shown in Figures 4–7.

#### 4. BP NEURAL Network Modeling

As discussed in Section 3, each combination of shear stiffnesses of the asphaltic bearings of U-shaped flumes ( $K_{flume}$ ), the dynamic elastic modulus of arch trusses ( $E_{d-arch}$ ) and the dynamic elastic modulus of bent frames and moment frame supports ( $E_{d-frame}$ ) will yield a set of primary modal frequencies of the aqueduct in three directions. So, according to the Universal Approximation Theorem of a feed-forward neural network [27],  $K_{flume}$ ,  $E_{d-arch}$  and  $E_{d-frame}$  of the aqueduct can be approximated with a BP neural network using the primary modal frequencies of the structure obtained from the in situ dynamic tests.

To fulfill the BP neural network modeling, a large number of modal analyses of the 3D aqueduct model need to be conducted to obtain the training data.

Using Equation (2), for a rubber bearing with  $A$  and  $t$  being  $250 \times 400 \text{ mm}^2$  and 2.0 mm, respectively, the shear modulus  $G$  can be taken as 1.2 MPa per the Chinese code “Laminated Bearing for Highway Bridge (JT/T 4-2019)”, and then the bearing shear stiffness would be calculated as  $6 \times 10^4 \text{ kN/m}$ . However, the asphaltic bearing material is not rubber, and its mechanical property is difficult to determine. Taking the hardened asphalt as a reference, the elastic modulus typically falls into a range from 1000 MPa to 9000 MPa, so the bearing shear stiffness could be several thousand times the rubber bearing. Considering other unknown factors,  $K_{flume}$  array is then formed using a geometric progression in a wide range from  $4.8 \times 10^5 \text{ kN/m}$  to  $1.2288 \times 10^8 \text{ kN/m}$  with a constant multiplier of 2, which contains 9 elements.  $E_{d-arch}$  and  $E_{d-frame}$  are taken from two arithmetic progressions from 35 GPa to 60 GPa and from 30 GPa to 55 GPa with a constant increment of 5, respectively, and 20 pairs are randomly selected. Each pair of  $E_{d-arch}$  and  $E_{d-frame}$  is combined with each element of the  $K_{flume}$  array, which leads to a total of 180 combinations.

These 180 combinations of  $K_{flume}$ ,  $E_{d-arch}$  and  $E_{d-frame}$  are put back into the 3D model individually to perform modal analyses, while the “m” value of foundation soil and the dynamic elastic modulus of pile caps and piles are taken as constant values (300 MN/m<sup>4</sup> and 35 GPa, respectively). Each combination will generate one set of primary modal frequencies of the aqueduct (i.e., the first, second and third lateral modes  $f_{T1}$ ,  $f_{T2}$  and  $f_{T3}$ , the first and second longitudinal modes  $f_{L1}$  and  $f_{L2}$ , and the first vertical mode  $f_{V1}$ ), which finally creates a dataset with 180 lines, and each line contains 9 elements, namely, the six inputs  $f_{T1}$ ,  $f_{T2}$ ,  $f_{T3}$ ,  $f_{L1}$ ,  $f_{L2}$ ,  $f_{V1}$  and three outputs  $K_{flume}$ ,  $E_{d-arch}$ ,  $E_{d-frame}$ .

In BP modeling, this total dataset is randomly divided into training, validation and testing sets with a division ratio of 8:1:1, so the sizes for the three sets are 144, 18 and

18, respectively. The validation set is employed to optimize the hyperparameters of the BP neural network (i.e., the number of hidden layers, the size of each hidden layer and the transfer function of each layer). Since the size of the training and validation dataset (180) is relatively small, a  $K$ -fold cross-validation process is utilized with  $K = 9$ . So, the BP neural network will be trained 9 times, and the average MSE (mean square error) and the average MAE (mean absolute relative error) of the 9 validations will be used to determine the optimal architecture of the network.

Since the ratio of the minimum input  $K_{flume}$  to its maximum value is only 1/256, it is found in the BP neural network pretraining that approximations are not satisfactory. So,  $K_{flume}$  in the total dataset is pretreated with natural logarithm, but even after this pretreatment, a BP neural network with just one hidden layer still gives rise to notable errors through the aforementioned 9-fold cross-validation process. So, a BP neural network with two hidden layers is employed, and when the neuron number for each hidden layer is 9, the cross-validation results for the transfer functions of the hidden and output layers are shown in Table 8, where case 6 gives the best approximation and quick convergence. Further investigation shows that when the neuron number of each hidden layer is decreased to 7 or increased to 11, the average MAE and MSE will not show any improvement.

**Table 8.** Cross validation of the hidden-layer 2 BP neural network.

| Case | Transfer Function |                |              | $E_{d-Arch}$ |                            | $E_{d-Frame}$ |                            | $\ln(K_{I-flume})$ |                               |
|------|-------------------|----------------|--------------|--------------|----------------------------|---------------|----------------------------|--------------------|-------------------------------|
|      | Hidden Layer 1    | Hidden Layer 2 | Output Layer | Avg. MAE     | Avg. MSE /GPa <sup>2</sup> | Avg. MAE      | Avg. MSE /GPa <sup>2</sup> | Avg. MAE           | Avg. MSE /(kN/m) <sup>2</sup> |
| 1    | purelin           | tansig         | tansig       | 0.25%        | 0.06                       | 0.36%         | 0.06                       | 0.58%              | 0.03                          |
| 2    | tansig            | tansig         | tansig       | 0.38%        | 0.29                       | 0.25%         | 0.07                       | 1.65%              | 0.39                          |
| 3    | purelin           | purelin        | tansig       | 2.25%        | 1.11                       | 2.30%         | 1.43                       | 16.54%             | 10.97                         |
| 4    | tansig            | purelin        | tansig       | 0.22%        | 0.09                       | 0.25%         | 0.12                       | 9.93%              | 5.94                          |
| 5    | tansig            | logsig         | tansig       | 0.25%        | 0.06                       | 0.20%         | 0.02                       | 0.72%              | 0.04                          |
| 6    | logsig            | logsig         | tansig       | 0.15%        | 0.02                       | 0.18%         | 0.03                       | 0.47%              | 0.02                          |
| 7    | tansig            | tansig         | logsig       | 13.1%        | 48.92                      | 6.98%         | 19.99                      | 6.85%              | 1.81                          |

MATLAB is used to perform the BP neural network modeling and approximation. The purelin, tansig and logsig transfer functions are illustrated as shown in Figure 16:

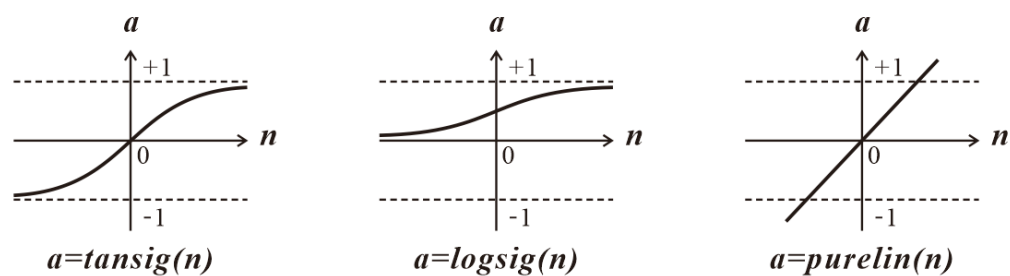


**Figure 16.** Illustration of transfer functions.

Therefore, it can be concluded that a BP neural network of which both the first and second hidden layers have 9 neurons with a transfer function of “logsig” and the output layer has 3 neurons with a transfer function of “tansig” can provide very good approximations for  $K_{flume}$ ,  $E_{d-arch}$  and  $E_{d-frame}$ . The final BP neural network for evaluating  $K_{flume}$ ,  $E_{d-arch}$  and  $E_{d-frame}$  is trained using this architecture with the training and validation dataset, and then the testing dataset is applied, which produces the following test results, as shown in Table 9.

**Table 9.** Test results of BP neural network with 6 frequency inputs.

| $E_{d\text{-}arch}$ |                      | $E_{d\text{-}frame}$ |                      | $Ln (K_{l\text{-}flume})$ |                         |
|---------------------|----------------------|----------------------|----------------------|---------------------------|-------------------------|
| MAE                 | MSE/GPa <sup>2</sup> | MAE                  | MSE/GPa <sup>2</sup> | MAE                       | MSE/(kN/m) <sup>2</sup> |
| 0.09%               | 0.003                | 0.19%                | 0.029                | 0.41%                     | 0.023                   |

Using the dynamic characteristics of the whole aqueduct obtained from field tests, as shown in Table 1, as the six inputs ( $f_{T1}$  0.97 Hz,  $f_{T2}$  1.02 Hz,  $f_{T3}$  1.06 Hz,  $f_{L1}$  1.50 Hz,  $f_{L2}$  1.915 Hz and  $f_{V1}$  5.328 Hz) of the trained BP neural network, the three outputs ( $K_{flume}$ ,  $E_{d\text{-}arch}$  and  $E_{d\text{-}frame}$ ) are estimated to be  $1.2288 \times 10^8$  kN/m, 47.8 GPa and 46.1 GPa, respectively. It should be noted that  $K_{flume}$  is approximated to be the maximum value of the corresponding training data, and this indicates that the asphaltic bearings of U-shaped flumes essentially behave more like a three-directional hinge which cannot provide effective dynamic isolation during seismic events.

Normally the first modes of the aqueduct in three directions are most prone to be excited when the structure is subjected to exterior dynamic loading, so technically they can be more easily and accurately detected by a field dynamic test than the other higher modes. If only such three frequencies as  $f_{T1}$ ,  $f_{L1}$  and  $f_{V1}$  are chosen as the inputs of the BP neural network of which the architecture still adopts the one specified by case 6 in Table 8, the modeling results of  $K_{flume}$ ,  $E_{d\text{-}arch}$  and  $E_{d\text{-}frame}$  using the same training and test procedures for Table 9 are shown in Table 10. It can be seen that a BP neural network with only 3 inputs ( $f_{T1}$ ,  $f_{L1}$  and  $f_{V1}$ ) is still capable of providing good approximations for  $K_{flume}$ ,  $E_{d\text{-}arch}$  and  $E_{d\text{-}frame}$ . By substituting the three first modes of the aqueduct in three directions ( $f_{T1}$  0.97 Hz,  $f_{L1}$  1.50 Hz and  $f_{V1}$  5.328 Hz) into the BP neural network specified in Table 10, the three outputs ( $K_{flume}$ ,  $E_{d\text{-}arch}$  and  $E_{d\text{-}frame}$ ) are estimated to be  $1.2288 \times 10^8$  kN/m, 48.1 GPa and 44.3 GPa, respectively. It can be seen that the BP neural networks with six and three inputs generate almost the same approximations for  $K_{flume}$  and  $E_{d\text{-}arch}$ , but the approximations for  $E_{d\text{-}frame}$  are somewhat different.

**Table 10.** Test results of BP neural network with 3 frequency inputs.

| $E_{d\text{-}arch}$ |                      | $E_{d\text{-}frame}$ |                      | $Ln (K_{l\text{-}flume})$ |                         |
|---------------------|----------------------|----------------------|----------------------|---------------------------|-------------------------|
| MAE                 | MSE/GPa <sup>2</sup> | MAE                  | MSE/GPa <sup>2</sup> | MAE                       | MSE/(kN/m) <sup>2</sup> |
| 0.12%               | 0.005                | 0.23%                | 0.049                | 1.06%                     | 0.069                   |

To evaluate which network could provide a better prediction, the three outputs ( $K_{flume}$ ,  $E_{d\text{-}arch}$  and  $E_{d\text{-}frame}$ ) obtained from those two BP neural networks are fed back into the 3D FE model to perform the modal analysis, and the results are shown in Tables 11 and 12.

**Table 11.** Comparison of frequencies obtained from field test and FE modal analysis using outputs of BP neural network with 6 frequency inputs.

| Modal Frequencies  | $f_{T1}/\text{Hz}$ | $f_{T2}/\text{Hz}$ | $f_{T3}/\text{Hz}$ | $f_{L1}/\text{Hz}$ | $f_{L2}/\text{Hz}$ | $f_{V1}/\text{Hz}$ |
|--------------------|--------------------|--------------------|--------------------|--------------------|--------------------|--------------------|
| Field test results | 0.970              | 1.020              | 1.060              | 1.500              | 1.915              | 5.328              |
| FE modal analysis  | 0.976              | 1.032              | 1.043              | 1.445              | 1.771              | 5.402              |
| Relative error     | 0.62%              | 1.18%              | -1.60%             | -3.67%             | -7.52%             | 1.39%              |

It can be seen that the FE modal analysis using  $K_{flume}$ ,  $E_{d\text{-}arch}$  and  $E_{d\text{-}frame}$  predicted by the BP neural network with six inputs generally show improved approximations to the main modal frequencies obtained from the in situ dynamic tests, especially for  $f_{L1}$  and  $f_{L2}$ , indicating that more input information on modal frequencies could enhance the prediction accuracy of the BP neural network.

**Table 12.** Comparison of frequencies obtained from field test and FE modal analysis using outputs of BP neural network with 3 frequency inputs.

| Modal Frequencies  | $f_{T1}/\text{Hz}$ | $f_{T2}/\text{Hz}$ | $f_{T3}/\text{Hz}$ | $f_{L1}/\text{Hz}$ | $f_{L2}/\text{Hz}$ | $f_{V1}/\text{Hz}$ |
|--------------------|--------------------|--------------------|--------------------|--------------------|--------------------|--------------------|
| Field test results | 0.970              | 1.020              | 1.060              | 1.500              | 1.915              | 5.328              |
| FE modal analysis  | 0.964              | 1.019              | 1.030              | 1.424              | 1.745              | 5.396              |
| Relative error     | −0.62%             | −0.10%             | −2.83%             | −5.07%             | −8.88%             | 1.28%              |

## 5. Conclusions

For the aqueduct under investigation in this study,  $K_{\text{flume}}$ ,  $E_{d\text{-arch}}$  and  $E_{d\text{-frame}}$  are among the main parameters to define its dynamic behavior, but there is no easy approach to get them tested directly on site. Since these parameters have direct correlation with the vibrational characteristics of the aqueduct, it is practicable to apply a BP neural network to evaluate them using the primary modal frequencies of the structure as inputs. However, it is impossible to obtain a large amount of experimental data to train the network from the real structure. To solve this data deficiency problem, a full-scale 3D FE model which can simulate the real structure to its best is established, and various modal analyses under different combinations of  $K_{\text{flume}}$ ,  $E_{d\text{-arch}}$  and  $E_{d\text{-frame}}$  are conducted to create the analytical dataset for the network. Through cross-validation procedure, the network architecture with two hidden layers is determined, and it shows that with appropriated transfer functions for the hidden and output layers, the trained BP neural network can provide very good approximations for  $K_{\text{flume}}$ ,  $E_{d\text{-arch}}$  and  $E_{d\text{-frame}}$  using the primary modal frequencies obtained from the FE model.

The actual primary modal frequencies acquired from in situ dynamic tests are then put into the BP neural network to estimate  $K_{\text{flume}}$ ,  $E_{d\text{-arch}}$  and  $E_{d\text{-frame}}$  of the aqueduct. By substituting the  $K_{\text{flume}}$ ,  $E_{d\text{-arch}}$  and  $E_{d\text{-frame}}$  obtained from two BP neural networks with different sizes (6 and 3) of input frequency vectors into the 3D FE model, it is found that more inputs of modal frequencies can improve the approximation accuracy of the BP neural network.

Finally the  $E_{d\text{-arch}}$  and  $E_{d\text{-frame}}$  of the aqueduct are approximated to be 47.8 GPa and 46.1 GPa, respectively, and  $K_{\text{flume}}$  is estimated to be the maximum value of the corresponding training data, implying that the makeshift asphaltic bearings of U-shaped flumes basically can be treated as a three-directional hinge (i.e., fixed in vertical, lateral and longitudinal translations) in the FE model.

**Author Contributions:** Conceptualization, X.L. (Xiaobin Lu) and X.L. (Xiulin Li); methodology, J.X.; software, M.L.; validation, X.L. (Xiaobin Lu) and M.L.; formal analysis, X.L. (Xiulin Li); investigation, J.X.; resources, X.L. (Xiaobin Lu); data curation, X.L. (Xiulin Li); writing—original draft preparation, X.L. (Xiaobin Lu); writing—review and editing, X.L. (Xiulin Li); visualization, J.X.; supervision, M.L.; project administration, X.L. (Xiaobin Lu); funding acquisition, X.L. (Xiaobin Lu). All authors have read and agreed to the published version of the manuscript.

**Funding:** This research was funded by the major science and technology project plan of the Ministry of Water Resources (SKS-2022111), IWR Research&Development Support Program (SM0145B022021) and the science and technology project of the Xinjiang Erqisi River Investment Development (Group) Co., Ltd. (QBT087/FY36).

**Institutional Review Board Statement:** Not applicable.

**Informed Consent Statement:** Not applicable.

**Data Availability Statement:** The data that support the findings of this study are available on request from the corresponding author.

**Acknowledgments:** “Research on static and dynamic safety monitoring and health evaluation for large aqueducts” sponsored by the Water Diversion Operation and Maintenance Center of Shandong Province.

**Conflicts of Interest:** The authors declare no conflict of interest.

## References

1. Mehta, P.K.; Monteiro, P.J. *Concrete: Microstructure, Properties, and Materials*; McGraw-Hill Education: New York, NY, USA, 2014.
2. Neville, A.M. *Properties of Concrete*, 5th ed.; Prentice-Hall/Pearson: San Francisco, CA, USA, 2012.
3. Brownjohn, J.M.; De Stefano, A.; Xu, Y.L.; Wenzel, H.; Aktan, A.E. Vibration-based monitoring of civil infrastructure: Challenges and successes. *J. Civ. Struct. Health Monit.* **2011**, *1*, 79–95. [[CrossRef](#)]
4. Ko, Y.Y.; Chang, W.K.; Liu, K.Y.; Hung, H.H.; Chang, K.C. Damage evaluation for RC bridge piers using vibration measurement. *Adv. Struct. Eng.* **2015**, *18*, 1501–1515. [[CrossRef](#)]
5. Chang, K.C.; Kim, C.W. Modal-parameter identification and vibration-based damage detection of a damaged steel truss bridge. *Eng. Struct.* **2016**, *122*, 156–173. [[CrossRef](#)]
6. Wang, T.; Celik, O.; Catbas, F.N. Damage detection of a bridge model based on operational dynamic strain measurements. *Adv. Struct. Eng.* **2016**, *19*, 1379–1389. [[CrossRef](#)]
7. Koto, Y.; Konishi, T.; Sekiya, H.; Miki, C. Monitoring local damage due to fatigue in plate girder bridge. *J. Sound Vib.* **2019**, *438*, 238–250. [[CrossRef](#)]
8. Ali, S.; Thambiratnam, D.; Fawzia, S.; Nguyen, K.D.; Van Den Elsen, H.; Fujii, I.A. Damage detection of an innovative composite slab-girder pedestrian bridge using vibration characteristics. *Struct. Infrastruct. Eng.* **2022**, *18*, 807–823. [[CrossRef](#)]
9. Walia, S.K.; Vinayak, H.K.; Kumar, A.; Parti, R. Modal parametric changes in a steel bridge with retrofitting. *Steel Compos. Struct.* **2015**, *19*, 385–403. [[CrossRef](#)]
10. Abe, M.; Fujino, Y. Monitoring of long-span bridges in Japan. *Proc. Inst. Civ. Eng.* **2017**, *170*, 135–144.
11. Farahani, R.V.; Penumadu, D. Damage identification of a full-scale five-girder bridge using time-series analysis of vibration data. *Eng. Struct.* **2016**, *115*, 129–139. [[CrossRef](#)]
12. Li, J.; Hao, H.; Xia, Y.; Zhu, H.P. Damage assessment of shear connectors with vibration measurements and power spectral density transmissibility. *Struct. Eng. Mech. Int. J.* **2015**, *54*, 257–289. [[CrossRef](#)]
13. Naito, H.; Bolander, J.E. Damage detection method for RC members using local vibration testing. *Eng. Struct.* **2019**, *178*, 361–374. [[CrossRef](#)]
14. Naito, H.; Sugiyama, R.; Bolander, J.E. Local vibration testing and damage evaluation for RC bridge decks. *J. Struct. Eng.* **2020**, *146*, 04020168. [[CrossRef](#)]
15. Shi, Z.; Hong, Y.; Yang, S. Updating boundary conditions for bridge structures using modal parameters. *Eng. Struct.* **2019**, *196*, 109346. [[CrossRef](#)]
16. Alves, V.; Cury, A.; Roitman, N.; Magluta, C.; Cremona, C. Structural modification assessment using supervised learning methods applied to vibration data. *Eng. Struct.* **2015**, *99*, 439–448. [[CrossRef](#)]
17. Nguyen, D.H.; Bui, T.T.; De Roeck, G.; Wahab, M.A. Damage detection in Ca-Non Bridge using transmissibility and artificial neural networks. *Struct. Eng. Mech.* **2019**, *71*, 175–183.
18. Jayasundara, N.; Thambiratnam, D.P.; Chan, T.H.T.; Nguyen, A. Locating and quantifying damage in deck type arch bridges using frequency response functions and artificial neural networks. *Int. J. Struct. Stab. Dyn.* **2020**, *20*, 2042010. [[CrossRef](#)]
19. Tan, Z.X.; Thambiratnam, D.P.; Chan, T.H.; Gordian, M.; Abdul Razak, H. Damage detection in steel-concrete composite bridge using vibration characteristics and artificial neural network. *Struct. Infrastruct. Eng.* **2020**, *16*, 1247–1261. [[CrossRef](#)]
20. Xu, L.H.; Yan, X.T.; Li, Z.X. Development of BP-based seismic behavior optimization of RC and steel frame structures. *Eng. Struct.* **2018**, *164*, 214–229. [[CrossRef](#)]
21. Huang, M.; Zhao, W.; Gu, J.; Lei, Y. Damage identification of a steel frame based on integration of time series and neural network under varying temperatures. *Adv. Civ. Eng.* **2020**, *2020*, 4284381. [[CrossRef](#)]
22. Cui, F.; Li, H.; Dong, X.; Wang, B.; Li, J.; Xue, H.; Qi, M. Improved time-dependent seismic fragility estimates for deteriorating RC bridge substructures exposed to chloride attack. *Adv. Struct. Eng.* **2021**, *24*, 437–452. [[CrossRef](#)]
23. Zhang, H.; Jin, C.; Zhang, X.; Ji, S.; Liu, X.; Li, X. Acoustic Emission Wavelet Analysis and Damage Stage Identification of Basalt Fiber-Reinforced Concrete under Dynamic Splitting Tensile Loads. *J. Mater. Civ. Eng.* **2023**, *35*, 04023147. [[CrossRef](#)]
24. Zhang, Y.; Miyamori, Y.; Mikami, S.; Saito, T. Vibration-based structural state identification by a 1-dimensional convolutional neural network. *Comput. Aided Civ. Infrastruct. Eng.* **2019**, *34*, 822–839. [[CrossRef](#)]
25. Nguyen, D.H.; Nguyen, Q.B.; Bui-Tien, T.; De Roeck, G.; Wahab, M.A. Damage detection in girder bridges using modal curvatures gapped smoothing method and Convolutional Neural Network: Application to Bo Nghi bridge. *Theor. Appl. Fract. Mech.* **2020**, *109*, 102728. [[CrossRef](#)]
26. *JGJ 94–2008; Technical Code for Building Pile Foundations*. China Architecture & Building Press: Beijing, China, 2008.
27. Hornik, K.; Stinchcombe, M.; White, H. Universal approximation of an unknown mapping and its derivatives using multilayer feedforward networks. *Neural Netw.* **1990**, *3*, 551–560. [[CrossRef](#)]

**Disclaimer/Publisher's Note:** The statements, opinions and data contained in all publications are solely those of the individual author(s) and contributor(s) and not of MDPI and/or the editor(s). MDPI and/or the editor(s) disclaim responsibility for any injury to people or property resulting from any ideas, methods, instructions or products referred to in the content.